energy&fuels

pubs.acs.org/EF Article

Selective Separation of CO_2 from Flue Gas Using Carbon and Boron Nitride Nanotubes as a Membrane

Manish Maurya, Praveen Kumar Sappidi, and Jayant K. Singh*

Cite This: *Energy Fuels* 2020, 34, 7223–7231 Read Online

ACCESS | Metrics & More | Article Recommendations

ABSTRACT: Molecular dynamics simulations are performed to study the separation of CO_2 from flue gas using carbon and boron nitride nanotube membranes. Flue gas is considered as a binary mixture of CO_2 and N_2 with CO_2 molar concentrations of 25 and 50%. Nanotubes of boron nitride and carbon with three different chiralities of (10,0), (14,0), and (18,0) are considered for the investigation of the effect of pore size on gas separation. The permeance of CO_2 is found to be higher in the boron nitride nanotube (BNNT) membrane compared to that in the carbon nanotube (CNT) membrane. The estimated CO_2 permeance is of the order of 10^7 GPU in both types of membranes at an initial applied pressure of 50 bar. The gas permeance decreases with a decrease in membrane pore size. The optimum pore size is determined on the basis of gas permeance and the corresponding selectivity data. The free-energy changes for N_2 molecules to pass through from the gas phase to the BNNT and CNT membranes are 19.36 and 9.06 kJ/mol, respectively, indicative of a significant barrier for N_2 permeance in the case of BNNT. Selectivity analysis also shows that the performance of boron nitride is better than that of carbon nanotube under same conditions. This work suggests that the direct use of boron nitride nanotube as a membrane can be useful for separating CO_2 from flue gas with high permeance.

INTRODUCTION

To mitigate the effect of global warming, it is urgent to capture major greenhouse gases, particularly CO_2, from the effluent gases of power plants and petrochemical industries. Different routes have been utilized to capture CO_2, such as postcombustion, precombustion, and oxy-fuel combustion. Among these routes, postcombustion CO_2 capture is the cheapest and easiest route to integrate into the existing plants. Several technologies are being investigated over the years for postcombustion CO_2 capture, including adsorption-, absorption-, membrane-, chemical looping-, and cryogenic distillation-based CO_2 separation.[1] Currently, the absorption technology is considered as the most suitable and mature technology for postcombustion CO_2 separation in power plants. Different solvents such as monoethanolamine (MEA), chilled ammonia, potassium carbonate, etc. have been employed for gas absorption technology since the 1980s.[2−4] These conventional amine-based absorption technologies are highly energy-intensive, and therefore, new types of solvents such as deep eutectic solvents and demixing solvents are being used for the more energy-efficient CO_2 separation process.[5−10] However, the absorption technique, despite being considered the most mature technology, has several drawbacks in terms of the formation of secondary pollutants, severe corrosion of equipment, loss of solvents, and high energy requirements in the regeneration process. This has motivated researchers worldwide to find alternative methods to capture CO_2.

Adsorption is another technique that can be used to capture CO_2 from flue gases using porous adsorbents. Different adsorbents such as zeolites, activated carbons, carbon nanotubes, metal−organic frameworks (MOFs), and covalent organic frameworks (COFs) have been used over the years to enhance the CO_2 adsorption capacity and selectivity.[11−23]

Membrane-based gas separation is an emerging technique that can also be an alternative to the absorption technology.[24,25] This technique is environmentally friendly and very energy-efficient compared to both the adsorption and absorption processes.[26] Membrane technology is extensively used for water treatment and gas separation.[27−29] Different types of membranes have been used for water treatment and gas separation, such as polymeric membranes, inorganic membranes, and mixed matrix membranes.[30−32] Polymeric membranes show high selectivity but very low permeability compared to porous materials.[33] There is a trade-off between selectivity and permeability in polymeric membranes.[34] Polymeric membranes cannot withstand high temperatures and extreme chemical environment, and they become swollen or plasticized when exposed to CO_2 or hydrocarbons with a high partial pressure. Inorganic polymers show tolerance to high temperature and extreme chemical environment, but they are very costly, brittle, and possess low membrane area.[26] Thus, membranes with high selectivity, high permeability, and stable structure under operating conditions are required.

Recently, two-dimensional (2D) materials are being extensively used as a membrane for gas separation to achieve

Received: January 29, 2020
Revised: May 5, 2020
Published: May 7, 2020

https://dx.doi.org/10.1021/acs.energyfuels.0c00311
Energy Fuels 2020, 34, 7223−7231

high selectivity and permeability. These 2D materials help achieve high throughput due to their ultrathin thickness. To date, a variety of 2D materials, such as graphene and its derivative[35−38] along with other materials such as boron nitride and its derivatives,[39−41] covalent organic frameworks (COFs),[42−45] metal−organic frameworks (MOFs),[46−48] and MoS_2,[49−51] have been widely used for gas separation, water desalination, and gas sensing applications. With these motivations, in this work, we have examined the utility of boron nitride nanotubes (BNNTs) and carbon nanotubes (CNTs) as a membrane instead of 2D sheets of graphene and boron nitride. We believe that an array of these nanotubes can potentially help in size-based gas separation and achieving a high rate of gas throughput. Different pore sizes of nanotubes provide different energy barriers to gas molecules at the entrance of the nanotube. Therefore, an optimum pore size will dictate the selective diffusion of gas molecules through the pores of nanotubes. This paper is organized as follows: First, the model of the system is introduced and then the gas permeation flux is studied with BNNT- and CNT-based membranes, followed by free-energy and selectivity analyses.

THEORY AND SIMULATION DETAILS

The structure of BNNTs is tubular in nature similar to carbon nanotubes, but carbon atoms are replaced with boron and nitrogen in a honeycomb lattice, as shown in Figure 1. Three

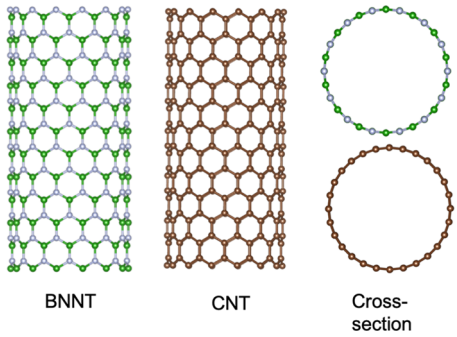

Figure 1. Axial and cross-sectional views of BNNT and CNT model structures.

armchair nanotubes of BNNT and CNT are considered in this work as a membrane. We have used structural chiralities of (18,0), (14,0), and (10,0) to achieve three different pore sizes of these nanotubes. A nanotube is kept in the middle of a 2D periodic simulation box of dimension 50.1 Å × 52.06 Å. We have considered a bichamber containing a gas side and a vacuum side separated by two surfaces. The nanotube is kept vertically embedded in these two surfaces at both ends, and gas molecules are inserted in the gas phase, as shown in Figure 2. The length of the nanotube is 25 Å. The dividing surface is modeled using a single sheet of graphene at both ends of the nanotubes having no interaction with the gas molecules. So, it is not possible for gas molecules to permeate through the hexagonal lattice of carbon atoms in the graphene sheet. To fit the nanotubes in the graphene sheet at both ends, defects of the size of nanotube's diameter are generated in both the sheets and the nanotubes are placed at a distance from the surface where the edges of nanotubes can form a bond with the surface molecules.

Flue gas is modeled as a binary mixture of CO_2 and N_2 as they represent the major fraction of the flue gas stream.

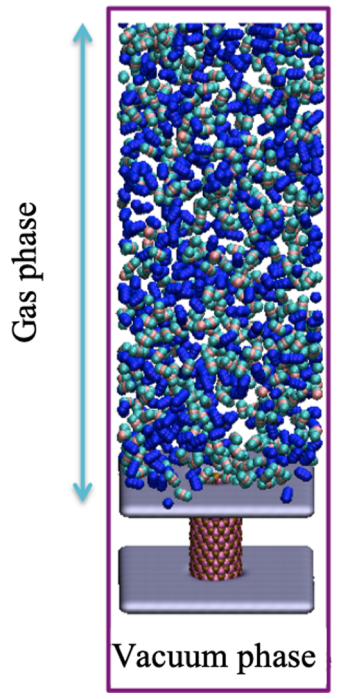

Figure 2. Simulation setup for a bichamber of equal volumes to separate CO_2 from the mixture of CO_2 and N_2. Nitrogen molecules are shown in blue, and CO_2 molecules are shown in cyan with pink. The gray color is used to denote two surfaces embedded with the nanotube.

Initially, the gas phase is filled with a mixture of CO_2 and N_2. A total of 2000 molecules are packed in the gas side with different concentrations (25 and 50 mol % corresponding to 500 and 1000 CO_2 molecules) of CO_2. The simulation box length in the z dimension is adjusted according to a pressure of 50 bar. The volume of the vacuum side is kept equal to that of the gas side. During simulations, the nanotube and two surfaces are considered to be rigid. The two surfaces dividing the gas phase and the vacuum phase are considered as a neutral wall with infinitesimally small van der Waals interaction (by reducing the energy potential well) with the gas molecules. On the other hand, CO_2 and N_2 are modeled as three-site rigid molecules with TraPPE potential. The force-field parameters of BNNT, CNT, and gas molecules are listed in Table 1.[52−54] The cross-interaction potential between different molecules (gas−gas and gas−nanotube) has been approximated by the Lorentz−Berthelot combining rules.[55]

Table 1. Force-Field Parameters for CO_2, N_2, BNNT, and CNT[a]

atom	σ (Å)	ϵ (kcal/mol)	q (e)
C	2.80	0.054	0.70
O	3.05	0.157	−0.35
N	3.31	0.072	−0.482
N (COM)	0.0	0.0	0.964
B	3.453	0.095	0.4
N^a	3.365	0.145	−0.4
C^a	3.4	0.056	0.0

[a] N^a and C^a represent the nitrogen atoms in BNNT and carbon atoms in CNT, respectively.

https://dx.doi.org/10.1021/acs.energyfuels.0c00311
Energy Fuels 2020, 34, 7223−7231

Molecular dynamics simulations are performed to study CO_2/N_2 separation using the nanotube membrane. Since the usual temperature of flue gas in power plant industries is 30−40 °C, the gas mixture in the gas phase is equilibrated first in the NVT ensemble for 1 ns at 303 K. After equilibration, the whole system is run in the NVT ensemble for 30 ns with a time step of 1 fs under the applied initial pressure gradient. The pressure gradient gradually changes with an increase in particle number in the vacuum part of the simulation box. The Nosè−Hoover thermostat is used to control the temperature of the system. The van der Waals interactions are truncated at 12 Å, and the long-range electrostatic interactions are measured by the PPPM Ewald method. All of the simulations are carried out using LAMMPS software.[56]

The thermodynamic integration method is used to calculate the change in the free energy of gas molecules. In this analysis, the free energy is calculated by considering potential energy as a function of a coupling parameter λ. As a consequence of this, Hamiltonian also becomes a function of λ, and further, the change in free energy between the two states of a system with $\lambda = 0$ (reference state) and $\lambda = 1$ (target state) can be calculated as follows[57]

$$\Delta F = F(\lambda = 1) - F(\lambda = 0) = \int_0^1 \left\langle \frac{\partial H(\lambda)}{\partial \lambda} \right\rangle_\lambda \mathrm{d}\lambda \quad (1)$$

where the angle brackets stand for ensemble average. At constant-temperature simulation, the kinetic-energy component of the Hamiltonian is not included in free-energy calculation. Therefore, the change in the Hamiltonian can be replaced by the change in the potential energy of the system. The integration must be performed along a reversible path from the reference state to the target state. In this formalism of free-energy calculation, the potential energy is assumed to be a linear function of coupling parameter as follows[58]

$$U(\lambda) = \lambda U_{\text{target}} + (1 - \lambda) U_{\text{reference}} \quad (2)$$

where U_{target} is the configurational energy of the target state and $U_{\text{reference}}$ is the configurational energy of the reference state. The total free energy (ΔF) is calculated using the two-stage thermodynamic integration method by the following expression

$$\Delta F = \Delta F_{\text{vdw}} + \Delta F_{\text{ele}} \quad (3)$$

where ΔF_{vdw} represents the contribution to the total binding free energy due to van der Waals interactions and ΔF_{ele} is the contribution to the total binding free energy due to electrostatic interactions. This can be further written as

$$\Delta F = \int_{(\lambda_{\text{vdw}=0}, \lambda_{\text{ele}=0})}^{\lambda_{\text{vdw}=1}, \lambda_{\text{ele}=0}} \left\langle \frac{\partial U(\lambda)}{\partial \lambda} \right\rangle_\lambda \mathrm{d}\lambda + \int_{(\lambda_{\text{vdw}=1}, \lambda_{\text{ele}=0})}^{\lambda_{\text{vdw}=1}, \lambda_{\text{ele}=1}} \left\langle \frac{\partial U(\lambda)}{\partial \lambda} \right\rangle_\lambda \mathrm{d}\lambda \quad (4)$$

where λ_{vdw} and λ_{ele} represent coupling parameters for van der Waals interaction and electrostatic interaction, respectively. In the first stage, we grow gas molecule (CO_2 or N_2) from the initial state with zero nonbonded interactions ($\lambda_{\text{vdw}} = \lambda_{\text{ele}} = 0$) to the final state with full van der Waals interactions ($\lambda_{\text{vdw}} = \lambda_{\text{ele}} = 1$). In the second stage, we grow it further to a state with full electrostatic and van der Waals interactions (i.e., $\lambda_{\text{vdw}} = 1$ and $\lambda_{\text{ele}} = 1$). We calculate $\frac{\partial U(\lambda)}{\partial \lambda}$ at each value of the coupling parameters in the range of 0.0−1.0. A total of 42 simulations (21 for ΔF_{vdw} and 21 for ΔF_{ele}) are performed to calculate the free energy. The thermodynamic cycle is presented in schematically in Figure 15. These free-energy simulations are performed using GROMACS.[59]

Gas permeation is defined as the number of gas molecules permeating to the other side of the membrane over time. The first derivative of the permeated molecules with time gives the rate of gas permeation, which is used to calculate the flux. The instantaneous gas permeation rate is calculated by fitting the simulated data using the following expression

$$N = A[1 - \exp(-t/B)] \quad (5)$$

where A and B are fitting constants. Since the permeance is generally reported in gas permeation unit (GPU) [1 GPU = 3.35×10^{-10} mol/(m^2 s Pa)], we take the first derivative of the number of permeated molecules divided by the cross-sectional area and Avogadro number to get instantaneous molar flux, which is further divided by pressure drop to get the flux in GPU unit. Ideal gas approximation is used to calculate the pressure of upstream and downstream gas molecules.

RESULTS AND DISCUSSION

Effect of Different Pore Sizes on Gas Permeation through the Membranes of BNNT and CNT. Figure 3 shows the permeation of CO_2 and N_2 molecules through the membranes of BNNT (18,0) and carbon nanotube (18,0). Figure 3a shows the performance of these membranes in the separation of CO_2 from the mixture of CO_2 and N_2 having a CO_2 concentration of 25%. The permeation of CO_2 is large compared to that of N_2 in both the membranes. The BNNT membrane shows a high CO_2 permeation compared to CNT. On the other hand, the permeation of N_2 is less in the BNNT membrane than in the CNT membrane. We further checked the separation of CO_2 from an equimolar mixture (50% CO_2) of CO_2 and N_2, as shown in Figure 3b. In the equimolar gas mixture, CO_2 permeation through both the membranes increases significantly due to the increased concentration of CO_2 in the mixture. As a result of the increased concentration of CO_2, which is preferably passing through the membrane, N_2 permeation decreases compared to the permeation of N_2 in the mixture containing 25% CO_2. The low permeation of N_2 in these two membranes can be attributed to its large kinetic diameter (3.64 Å) compared to the kinetic diameter of CO_2 (3.3 Å). Moreover, the formation of adsorbed CO_2 layer inside the nanotube also acts as a barrier for N_2 molecules. The approximate pore sizes of these nanotube membranes are 14,

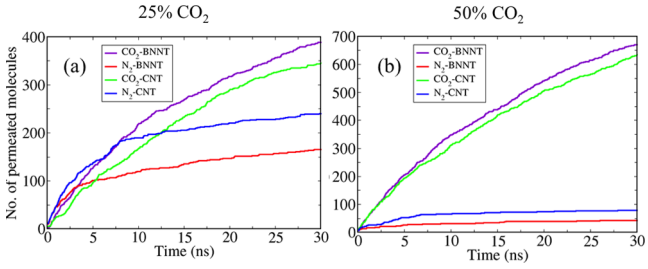

Figure 3. Permeation of gas molecules through the (18,0) nanotube membranes from a binary mixture of CO_2 and N_2 with (a) 25% CO_2 concentration and (b) 50% CO_2 concentration at an initial pressure of 50 bar and 303 K.

https://dx.doi.org/10.1021/acs.energyfuels.0c00311
Energy Fuels 2020, 34, 7223−7231

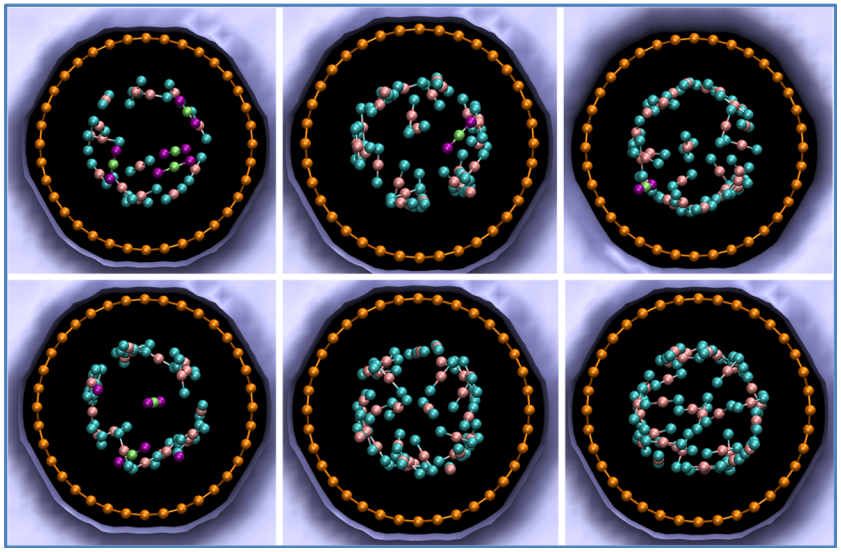

Figure 4. Formation of adsorbed CO_2 layer inside the BNNT membrane for the binary mixtures (25% CO_2, top; 50 % CO_2, bottom) of CO_2 and N_2 at different simulation times. CO_2 molecules are shown in cyan with pink, while N_2 molecules are shown in purple with green.

11, and 8 Å, respectively, which correspond to the chiralities of (18,0), (14,0), and (10,0). The snapshots of adsorbed CO_2 molecules for both binary mixtures are shown in Figure 4. The layer formed inside the nanotube hinders the diffusion of both CO_2 and N_2 molecules. The resistance is higher for N_2 because of its larger size. The snapshots show that only a few N_2 molecules are present in the layer. Therefore, the permeation of N_2 takes place only through the center of the nanotube and not along the walls as in the case of CO_2. The layer thickens with time and concentration of the mixture. As a result, in an equimolar mixture, there is a strong repulsion for N_2 molecules, which reduces its permeation flux. The formation of an adsorbed CO_2 layer reduces the effective pore size of the membranes. However, a complete rejection of N_2 molecules is not observed in these membranes.

We further investigated the gas permeation using smaller pore sizes (corresponding to structural chiralities of (14,0) and (10,0)) of the membranes. Figures 5 and6 show the

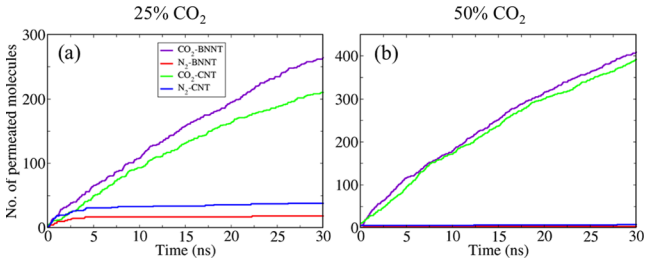

Figure 5. Permeation of gas molecules through (14,0) nanotube membranes from a binary mixture of CO_2 and N_2 with (a) 25% CO_2 concentration and (b) 50% CO_2 concentration at an initial pressure of 50 bar and 303 K.

permeation of gas molecules through the membranes with pore sizes of approximately 11 and 8 Å, respectively. The amount of gas permeation reduces with reducing pore size of the nanotube membranes. The smaller pore size of nanotubes significantly reduces the N_2 permeation in comparison to a large pore size of the membrane. In the case of a mixture containing 25% CO_2, as shown in Figure 6a, the permeation of

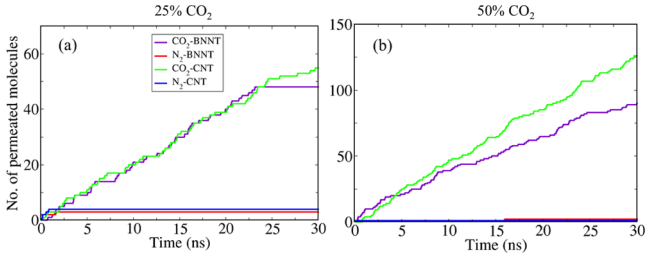

Figure 6. Permeation of gas molecules through (10,0) nanotube membranes from a binary mixture of CO_2 and N_2 with (a) 25% CO_2 concentration and (b) 50% CO_2 concentration at an initial pressure of 50 bar and 303 K.

CO_2 through the CNT is approximately similar to that observed through the BNNT membrane. This is because the adsorbed CO_2 layer in the smaller pore size of BNNT provides more resistance to permeating gas molecules compared to the small pore size of the CNT membrane. As a result of this, in an equimolar mixture of CO_2 and N_2 (Figure 6b), the permeation of CO_2 through CNT becomes higher than that of the permeation through BNNT. The gas molecules permeated through the BNNT and CNT membranes are shown in Figure 7. Figure 7a shows the gas permeation through the (18,0) BNNT membrane from a mixture of 25% CO_2 concentration at three different times. Over time, the permeation of gas molecules increases. A similar behavior is observed in the case of the (18,0) CNT membrane, as shown in Figure 7b. These snapshots show that the permeation of N_2 through the CNT membrane is higher than that through the BNNT membrane.

The effect of gas concentrations in the mixture on gas permeation through the BNNT membranes is shown in Figure 8. Figure 8a shows the gas permeation in a mixture of 50% CO_2 concentration, where N_2 permeation is very low compared to the permeation in the mixture containing 25% CO_2, as shown in Figure 8b. A typical snapshot of gas permeation is shown in Figure 8a,8b for two different gas mixtures. It is clearly evident from Figure 8a,8b that N_2 permeation is very low in the gas mixture containing 50% CO_2 compared to 25% CO_2.

https://dx.doi.org/10.1021/acs.energyfuels.0c00311
Energy Fuels 2020, 34, 7223−7231

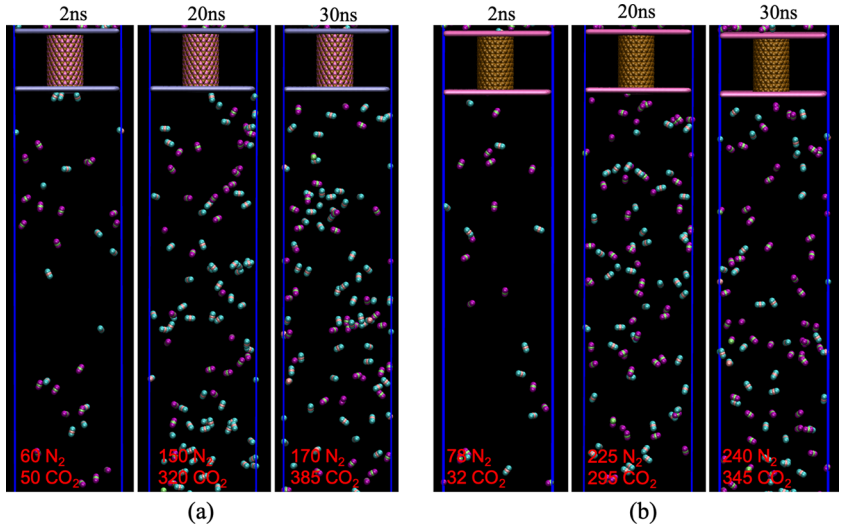

Figure 7. Snapshot of gas permeation through (a) (18,0) BNNT and (b) (18,0) CNT membranes from the binary mixture of CO_2 and N_2 having 25% CO_2 concentration. Snapshots are shown for three different times: 2, 20, and 30 ns. The gas and vacuum phases are truncated for the clarity of the image. CO_2 molecules are shown in cyan and pink, while N_2 molecules are shown in purple and green.

Free-Energy Barrier Analysis of Gas Permeation. To understand the reason behind the preferred permeation of CO_2 through both the membranes, we have calculated the change in free energy of CO_2 and N_2 molecules as it passes from bulk phase to inside the matrix of membrane. The changes in free energy for both the gas molecules are listed in Table 2. The change in free energy is favorable for CO_2 permeation through both the membranes, while for N_2, it shows a positive change in free energy, which indicates that both the membranes oppose the permeation of N_2 from the mixture of gases through its matrix. CNT shows a more favorable change in free energy for CO_2 than in BNNT. However, its resistance to N_2 permeation is not much compared to BNNT; as a result of this, the overall permeation of CO_2 in CNT is less than that of the BNNT membrane. Figure 9 shows the thermodynamic integration analysis to calculate the free energy. The contribution of van der Waals interaction potential to the free energy is shown in Figure 9a, which changes by changing the coupling parameter λ from 0 to 1. Figure 9b shows the contribution of electrostatic potential to free energy as a function of the coupling parameter. When we integrate these curves, we obtained individual electrostatic and van der Waals contribution for the total binding free energy. The ΔF_{vdw} value for CO_2 is -5.12 ± 0.53 kJ/mol in BNNT and -8.37 ± 0.34 kJ/mol in CNT; similarly, for N_2, it is 20.76 ± 0.95 kJ/mol in BNNT and 10.00 ± 0.74 kJ/mol in CNT. These ΔF_{vdw} show a favorable value for binding of CO_2 in CNT than BNNT, unfavorable for the binding of N_2 either in CNT or BNNT. On the other hand, the ΔF_{ele} value for CO_2 is -0.71 ± 0.05 kJ/mol in BNNT and -0.12 ± 0.05 kJ/mol in CNT; similarly, for N_2, it is -1.4 ± 0.33 kJ/mol in BNNT and -0.94 ± 0.34 kJ/mol in CNT. Interestingly, we see that ΔF_{ele} is slightly more favorable for binding N_2 than CO_2 in both CNT and BNNT. This could be due to the possible charged B and N atoms on BNNT. It is observed that the van der Waals contributions to the total binding free-energy values show more favorable binding of CO_2 in CNT than BNNT. However, its resistance to N_2 permeation is not much compared to BNNT; as a result of this, the overall permeation of CO_2 in CNT is less than that of the BNNT membrane. This is one of the key factors that cause the difference in the number of permeated CO_2 molecules between BNNT and CNT nanotube membranes.

Selectivity and Flux Analysis. Now, we turn our attention to the selectivity and gas permeance analysis through the membranes. To calculate the instantaneous flux of gas permeation, the number of permeated gas molecules is recorded with time and fitted with eq 5, as shown in Figure 10. The rate of permeated gas molecules is fitted to get a continuous curve, which is required to calculate the molar flux in both the membranes. Figure 11a shows the molar flux of CO_2 through the BNNT membrane. The initial molar flux of CO_2 permeation up to 5 ns is approximately 90% higher in the equimolar mixture than a mixture of 25% CO_2. It further decreases as the pressure gradient keeps decreasing due to the permeation of gas molecules to the vacuum side. A similar trend is observed in the CNT membrane too, as shown in Figure 11b, with the same pore size (18,0), but the magnitude of the permeated gas flux is less than that of the BNNT membrane. However, the CO_2 permeance is of the order of 10^7 GPU in both the membranes having a pore size of ≈14 Å that is higher than some reported gas permeance data at and around this temperature and pressure conditions. Jafar et al. showed that the functionalized 2D boron nitride sheet shows CO_2 permeance of the order of 10^4 GPU in an equimolar binary mixture of CO_2 and N_2 at a pressure of about 62 bar.[60] In another study where windowed carbon nanotube is used for natural gas sweetening by separating CO_2 from methane, they reported that the CO_2 permeance is of the order of 10^7 GPU at 180 bar.[61] Most of the 2D membranes have CO_2 permeance of the order of 10^4–10^6 GPU at different pressure conditions.[62,63] We further checked the effect of membrane pore size on the gas permeance by reducing it to an intermediate pore size of 11 Å, which corresponds to a structural chirality of (14,0), as shown in Figure 12. The gas permeation is observed to decrease compared to a pore size of 14 Å in both the membranes. Further reduction in pore size reduces the gas permeation flux by a factor of 10 in BNNT and CNTs, as shown in Figure 13. Since 25% gas mixture is close to the actual binary composition of flue gas (15% CO_2 and 80% N_2), we showed a comparison of mixture having 25% CO_2

https://dx.doi.org/10.1021/acs.energyfuels.0c00311
Energy Fuels 2020, 34, 7223−7231

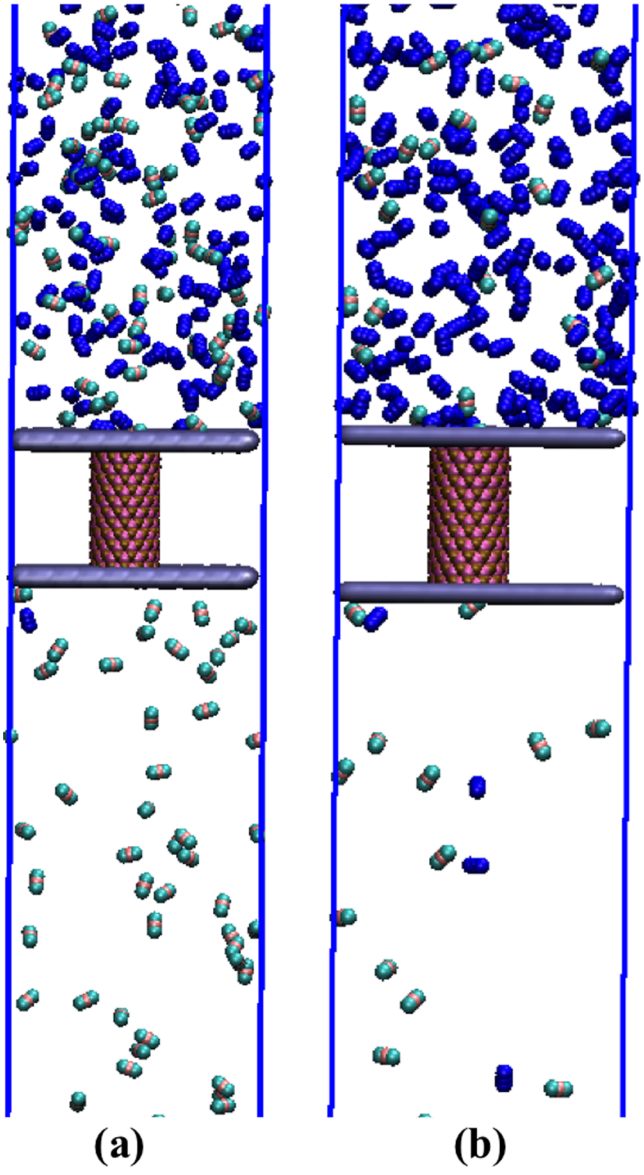

Figure 8. Snapshot of gas permeation through the (14,0) BNNT membrane from a binary mixture of CO_2 and N_2 with (a) 50% CO_2 concentration and (b) 25% CO_2 concentration.

Table 2. Change in Free Energy of CO_2 and N_2 in (14,0) CNT and BNNT Membranes at 303 K and 50 bar

membrane	ΔF_{CO_2} (kJ/mol)	ΔF_{N_2} (kJ/mol)
BNNT	−5.83 ± 0.58	19.36 ± 1.28
CNT	−8.49 ± 0.39	9.06 ± 1.18

concentration in BNNT and CNT membranes in Figure 13. However, we expect a similar trend in the flux for other compositions. Though the flux reduces, it is still comparable to those of other 2D materials in this pressure range (50 bar).[60] The decay rate of gas permeation is high in BNNT compared to CNT irrespective of the pore size of these membranes.

Apart from high gas permeability, the selectivity of a membrane is equally important in the membrane-based gas separation. Therefore, in this regard, we have checked the selectivities of BNNT and CNT membranes for CO_2 molecules. Figure 14a–c shows the performance of the nanotube membranes based on the selectivity data. The

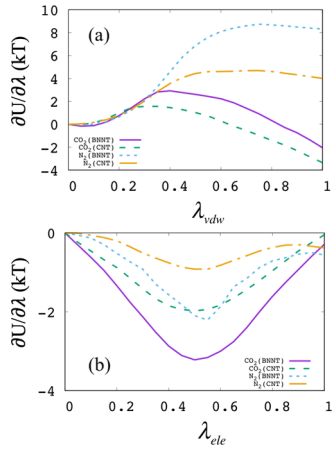

Figure 9. Thermodynamic integration analysis for the gas molecules with CNT and BNNT membranes. The partial derivative of potential energy with respect to (wrt) a coupling parameter is shown in two parts: (a) contribution of van der Waals interactions and (b) contribution of electrostatic interactions.

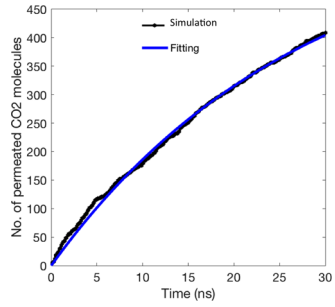

Figure 10. Fitting of permeated CO_2 molecules in simulation with analytical expression.

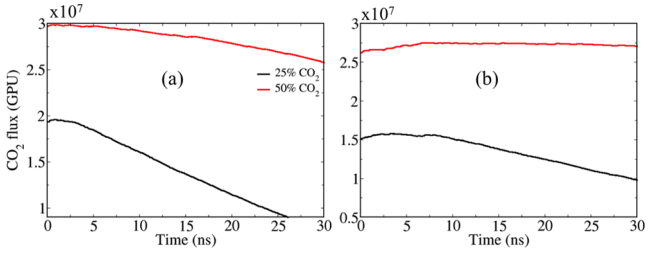

Figure 11. Permeance of CO_2 through (a) (18,0) BNNT and (b) (18,0) CNT membranes at 303 K.

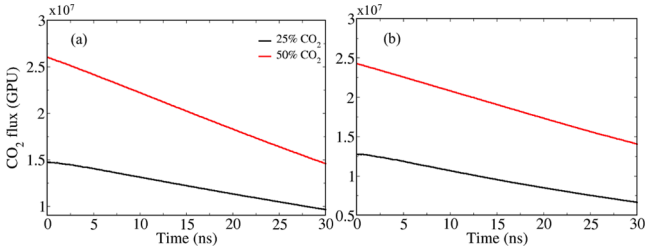

Figure 12. Permeance of CO_2 through (a) (14,0) BNNT and (b) (14,0) CNT membranes at 303 K.

selectivity data show that the performance of the BNNT-based membrane is better than that of the CNT-based membrane in three different pore sizes. The selective permeation depends on the pore size of the membranes. There is a trade-off between

https://dx.doi.org/10.1021/acs.energyfuels.0c00311
Energy Fuels 2020, 34, 7223−7231

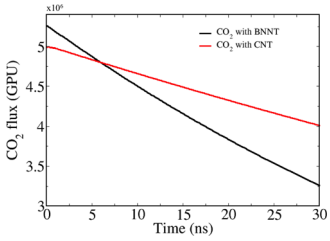

Figure 13. Permeance of CO_2 through (10,0) BNNT and CNT membranes from a mixture of 25% CO_2 at 303 K.

gas permeation flux and selectivity. Among different pores and types of membranes considered in this work, on the basis of permeation flux and selectivity data, the (14,0) BNNT membrane shows better performance for selective gas separation than the CNT-based membrane (Figure 15).

CONCLUSIONS

In this work, molecular dynamics simulations are performed to study the membrane-based gas separation. Nanotubes of BNNT and CNT with three different chiralities of (18,0), (14,0), and (10,0) are considered as a membrane for gas separation. Flue gas is considered as a mixture of CO_2 and N_2 with CO_2 concentrations of 25 and 50%. The molecular dynamics results show that the permeation flux of CO_2 through different membranes is a function of membrane pore size. The gas permeation reduces by reducing the pore size. There is a slight resistance for N_2 permeation in large pores of membranes corresponding to a chirality of (18,0). An intermediate pore size, with chirality of (14,0), shows an optimum result for gas permeance and selectivity. The performance of the (14,0) BNNT membrane is found to be better than that of the (14,0) CNT membrane. The order of gas permeance in (14,0) BNNT and CNT is 10^7 GPU, which decreases by a factor of 10 upon reducing the pore size to ≈8 Å corresponding to the (10,0) chirality. The gas permeation flux is found to decrease with a decrease in pore size of both the membranes, while the selectivity is higher for intermediate pore sizes. The change in free energy suggests that the permeation of CO_2 through CNT is more favorable than through BNNT, but at the same time, it also indicates that the resistance for N_2 permeation through CNT is less than that through BNNT, and hence, it reduces the overall permeation of CO_2 through the CNT membrane than through the BNNT membrane. Thus, the BNNT-based membrane shows more selective permeation of CO_2. It is found that the permeation of N_2 is strongly opposed by both BNNT and CNT membranes. The selectivity analysis also reveals that the (14,0) BNNT is better than the CNT membrane for gas separation with high permeability.

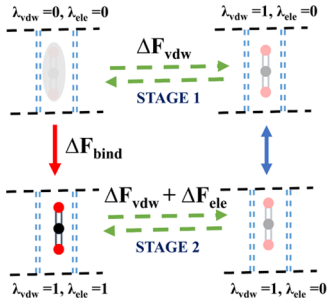

Figure 15. Schematic representation of thermodynamic cycle for calculating the binding free energy.

AUTHOR INFORMATION

Corresponding Author

Jayant K. Singh − *Department of Chemical Engineering, Indian Institute of Technology, Kanpur 208016, India;* orcid.org/0000-0001-8056-2115; Email: jayantks@iitk.ac.in

Authors

Manish Maurya − *Department of Chemical Engineering, Indian Institute of Technology, Kanpur 208016, India*

Praveen Kumar Sappidi − *Department of Chemical Engineering, Indian Institute of Technology, Kanpur 208016, India*

Complete contact information is available at: https://pubs.acs.org/10.1021/acs.energyfuels.0c00311

Notes

The authors declare no competing financial interest.

ACKNOWLEDGMENTS

The authors thank the high-performance computational facility of IIT Kanpur for all of the computational facilities and the Ministry of Human Resource and Development, Govt. of India, for all of the funding.

REFERENCES

(1) Tuinier, M. J.; van Sint Annaland, M.; Kramer, G.; Kuipers, J. Cryogenic CO_2 capture using dynamically operated packed beds. *Chem. Eng. Sci.* **2010**, *65*, 114−119. 20th International Symposium in Chemical Reaction Engineering—Green Chemical Reaction Engineering for a Sustainable Future.

(2) Kothandaraman, A.; Nord, L.; Bolland, O.; Herzog, H. J.; McRae, G. J. Comparison of Solvents for Post-combustion Capture of

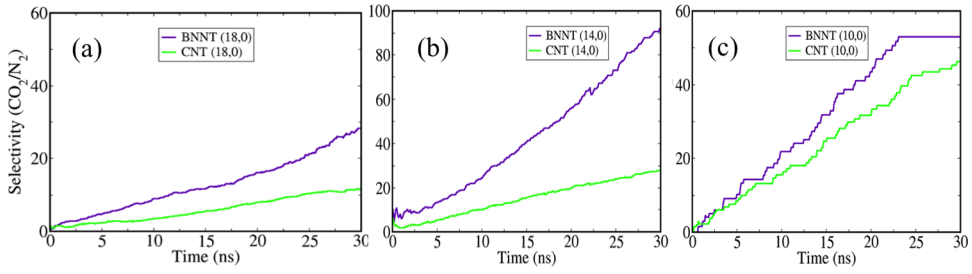

Figure 14. Selectivity analysis of CO_2 over N_2 in a binary mixture of CO_2/N_2 with 25% CO_2 concentration using (a) (18,0) nanotubes, (b) (14,0) nanotubes, and (c) (10,0) nanotubes of boron nitride and carbon.

https://dx.doi.org/10.1021/acs.energyfuels.0c00311
Energy Fuels 2020, 34, 7223−7231

CO_2 by Chemical Absorption. *Energy Procedia* **2009**, *1*, 1373−1380. Greenhouse Gas Control Technologies 9.
(3) Dutcher, B.; Fan, M.; Russell, A. G. Amine-Based CO_2 Capture Technology Development from the Beginning of 2013—A Review. *ACS Appl. Mater. Interfaces* **2015**, *7*, 2137−2148.
(4) Luis, P. Use of monoethanolamine (MEA) for CO_2 capture in a global scenario: Consequences and alternatives. *Desalination* **2016**, *380*, 93−99.
(5) García, G.; Aparicio, S.; Ullah, R.; Atilhan, M. Deep Eutectic Solvents: Physicochemical Properties and Gas Separation Applications. *Energy Fuels* **2015**, *29*, 2616−2644.
(6) Lin, H.; Gong, K.; Ying, W.; Chen, D.; Zhang, J.; Yan, Y.; Peng, X. CO_2-Philic Separation Membrane: Deep Eutectic Solvent Filled Graphene Oxide Nanoslits. *Small* **2019**, *15*, No. 1904145.
(7) Raynal, L.; Bouillon, P.-A.; Gomez, A.; Broutin, P. From MEA to Demixing Solvents and Future steps, A Roadmap for Lowering the Cost of Post-combustion Carbon Capture. *Chem. Eng. J.* **2011**, *171*, 742−752. Special Section: Symposium on Post-Combustion Carbon Dioxide Capture.
(8) Coulier, Y.; Lowe, A. R.; Coxam, J.-Y.; Ballerat-Busserolles, K. Thermodynamic Modeling and Experimental Study of CO_2 Dissolution in New Absorbents for Post-Combustion CO_2 Capture Processes. *ACS Sustainable Chem. Eng.* **2018**, *6*, 918−926.
(9) Campbell, M. Technology Innovation & Advancements for Shell Cansolv CO_2 capture solvents. *Energy Procedia* **2014**, *63*, 801−807.
(10) Kadono, K.; Suzuki, A.; Iijima, M.; Ohishi, T.; Tanaka, H.; Hirata, T.; Kondo, M. New Energy Efficient Processes and Newly Developed Absorbents for Flue Gas CO_2 Capture. *Energy Procedia* **2013**, *37*, 1785−1792. GHGT-11 Proceedings of the 11th International Conference on Greenhouse Gas Control Technologies, 18-22 November 2012, Kyoto, Japan.
(11) Pirngruber, G. D.; Raybaud, P.; Belmabkhout, Y.; Čejka, J.; Zukal, A. The role of the extra-framework cations in the adsorption of CO_2 on faujasite Y. *Phys. Chem. Chem. Phys.* **2010**, *12*, 13534−13546.
(12) Cavenati, S.; Grande, C. A.; Rodrigues, A. E. Adsorption Equilibrium of Methane, Carbon Dioxide, and Nitrogen on Zeolite 13X at High Pressures. *J. Chem. Eng. Data* **2004**, *49*, 1095−1101.
(13) Na, B.-K.; Koo, K.-K.; Eum, H.-M.; Lee, H.; Song, H. K. CO_2 recovery from flue gas by PSA process using activated carbon. *Korean J. Chem. Eng.* **2001**, *18*, 220−227.
(14) Rahimi, M.; Babu, D. J.; Singh, J. K.; Yang, Y.-B.; Schneider, J. J.; Müller-Plathe, F. Double-walled carbon nanotube array for CO_2 and SO_2 adsorption. *J. Chem. Phys.* **2015**, *143*, No. 124701.
(15) Majumdar, S.; Maurya, M.; Singh, J. K. Adsorptive Separation of CO_2 from Multicomponent Mixtures of Flue Gas in Carbon Nanotube Arrays: A Grand Canonical Monte Carlo Study. *Energy Fuels* **2018**, *32*, 6090−6097.
(16) Halder, P.; Maurya, M.; Jain, S. K.; Singh, J. K. Understanding adsorption of CO_2, N_2, CH_4 and their mixtures in functionalized carbon nanopipe arrays. *Phys. Chem. Chem. Phys.* **2016**, *18*, 14007−14016.
(17) Maurya, M.; Singh, J. K. A grand canonical Monte Carlo study of SO_2 capture using functionalized bilayer graphene nanoribbons. *J. Chem. Phys.* **2017**, *146*, No. 044704.
(18) Maurya, M.; Singh, J. K. Treatment of Flue Gas using Graphene Sponge: A Simulation Study. *J. Phys. Chem. C* **2018**, *122*, 14654−14664.
(19) Vicent-Luna, J. M.; Gutiérrez-Sevillano, J. J.; Anta, J. A.; Calero, S. Effect of Room-Temperature Ionic Liquids on CO_2 Separation by a Cu-BTC Metal-Organic Framework. *J. Phys. Chem. C* **2013**, *117*, 20762−20768.
(20) Simmons, J. M.; Wu, H.; Zhou, W.; Yildirim, T. Carbon capture in metal-organic frameworks−a comparative study. *Energy Environ. Sci.* **2011**, *4*, 2177−2185.
(21) Caskey, S. R.; Wong-Foy, A. G.; Matzger, A. J. Dramatic Tuning of Carbon Dioxide Uptake via Metal Substitution in a Coordination Polymer with Cylindrical Pores. *J. Am. Chem. Soc.* **2008**, *130*, 10870−10871.
(22) Ding, S.-Y.; Wang, W. Covalent organic frameworks (COFs): from design to applications. *Chem. Soc. Rev.* **2013**, *42*, 548−568.
(23) Babarao, R.; Jiang, J. Exceptionally high CO_2 storage in covalent-organic frameworks: Atomistic simulation study. *Energy Environ. Sci.* **2008**, *1*, 139−143.
(24) Sedigh, M. G.; Onstot, W. J.; Xu, L.; Peng, W. L.; Tsotsis, T. T.; Sahimi, M. Experiments and Simulation of Transport and Separation of Gas Mixtures in Carbon Molecular Sieve Membranes. *J. Phys. Chem. A* **1998**, *102*, 8580−8589.
(25) Ockwig, N. W.; Nenoff, T. M. Membranes for Hydrogen Separation. *Chem. Rev.* **2007**, *107*, 4078−4110.
(26) Bernardo, P.; Drioli, E.; Golemme, G. Membrane Gas Separation: A Review/State of the Art. *Ind. Eng. Chem. Res.* **2009**, *48*, 4638−4663.
(27) Cséfalvay, E.; Pauer, V.; Mizsey, P. Recovery of copper from process waters by nanofiltration and reverse osmosis. *Desalination* **2009**, *240*, 132−142. The Third Membrane Science and Technology Conference of Visegrad Countries (PERMEA); part 1.
(28) Wang, R.; Guan, S.; Sato, A.; Wang, X.; Wang, Z.; Yang, R.; Hsiao, B. S.; Chu, B. Nanofibrous microfiltration membranes capable of removing bacteria, viruses and heavy metal ions. *J. Membr. Sci.* **2013**, *446*, 376−382.
(29) Brunetti, A.; Scura, F.; Barbieri, G.; Drioli, E. Membrane technologies for CO_2 separation. *J. Membr. Sci.* **2010**, *359*, 115−125. Membranes and CO_2 Separation.
(30) Budd, P. M.; Msayib, K. J.; Tattershall, C. E.; Ghanem, B. S.; Reynolds, K. J.; McKeown, N. B.; Fritsch, D. Gas separation membranes from polymers of intrinsic microporosity. *J. Membr. Sci.* **2005**, *251*, 263−269.
(31) Sanders, D. F.; Smith, Z. P.; Guo, R.; Robeson, L. M.; McGrath, J. E.; Paul, D. R.; Freeman, B. D. Energy-efficient polymeric gas separation membranes for a sustainable future: A review. *Polymer* **2013**, *54*, 4729−4761.
(32) Prabhakar, R. S.; Freeman, B. D.; Roman, I. Gas and Vapor Sorption and Permeation in Poly(2,2,4-trifluoro-5-trifluoromethoxy-1,3-dioxole-co-tetrafluoroethylene). *Macromolecules* **2004**, *37*, 7688−7697.
(33) Robeson, L. M. Correlation of separation factor versus permeability for polymeric membranes. *J. Membr. Sci.* **1991**, *62*, 165−185.
(34) Robeson, L. M. The upper bound revisited. *J. Membr. Sci.* **2008**, *320*, 390−400.
(35) Li, H.; Song, Z.; Zhang, X.; Huang, Y.; Li, S.; Mao, Y.; Ploehn, H. J.; Bao, Y.; Yu, M. Ultrathin, Molecular-Sieving Graphene Oxide Membranes for Selective Hydrogen Separation. *Science* **2013**, *342*, 95−98.
(36) Tian, Z.; Mahurin, S. M.; Dai, S.; Jiang, D.-e. Ion-Gated Gas Separation through Porous Graphene. *Nano Lett.* **2017**, *17*, 1802−1807.
(37) Jiang, D.-e.; Cooper, V. R.; Dai, S. Porous Graphene as the Ultimate Membrane for Gas Separation. *Nano Lett.* **2009**, *9*, 4019−4024.
(38) Sun, P.; Wang, K.; Zhu, H. Recent Developments in Graphene-Based Membranes: Structure, Mass-Transport Mechanism and Potential Applications. *Adv. Mater.* **2016**, *28*, 2287−2310.
(39) Azamat, J.; Khataee, A.; Joo, S. W. Removal of heavy metals from water through armchair carbon and boron nitride nanotubes: a computer simulation study. *RSC Adv.* **2015**, *5*, 25097−25104.
(40) Darvish Ganji, M.; Dodangeh, R. Hydrogen purification performance of a nanoporous hexagonal boron nitride membrane: molecular dynamics and first-principle simulations. *Phys. Chem. Chem. Phys.* **2017**, *19*, 12032−12044.
(41) Gao, H.; Shi, Q.; Rao, D.; Zhang, Y.; Su, J.; Liu, Y.; Wang, Y.; Deng, K.; Lu, R. Rational Design and Strain Engineering of Nanoporous Boron Nitride Nanosheet Membranes for Water Desalination. *J. Phys. Chem. C* **2017**, *121*, 22105−22113.
(42) Tong, M.; Yang, Q.; Ma, Q.; Liu, D.; Zhong, C. Few-layered ultrathin covalent organic framework membranes for gas separation: a computational study. *J. Mater. Chem. A* **2016**, *4*, 124−131.

https://dx.doi.org/10.1021/acs.energyfuels.0c00311
Energy Fuels 2020, 34, 7223−7231

(43) Fan, H.; Mundstock, A.; Feldhoff, A.; Knebel, A.; Gu, J.; Meng, H.; Caro, J. Covalent Organic Framework-Covalent Organic Framework Bilayer Membranes for Highly Selective Gas Separation. *J. Am. Chem. Soc.* **2018**, *140*, 10094−10098.
(44) Chandra, S.; Kandambeth, S.; Biswal, B. P.; Lukose, B.; Kunjir, S. M.; Chaudhary, M.; Babarao, R.; Heine, T.; Banerjee, R. Chemically Stable Multilayered Covalent Organic Nanosheets from Covalent Organic Frameworks via Mechanical Delamination. *J. Am. Chem. Soc.* **2013**, *135*, 17853−17861.
(45) Li, G.; Zhang, K.; Tsuru, T. Two-Dimensional Covalent Organic Framework (COF) Membranes Fabricated via the Assembly of Exfoliated COF Nanosheets. *ACS Appl. Mater. Interfaces* **2017**, *9*, 8433−8436.
(46) Zhao, M.; Wang, Y.; Ma, Q.; Huang, Y.; Zhang, X.; Ping, J.; Zhang, Z.; Lu, Q.; Yu, Y.; Xu, H.; et al. Ultrathin 2D Metal-Organic Framework Nanosheets. *Adv. Mater.* **2015**, *27*, 7372−7378.
(47) Peng, Y.; Li, Y.; Ban, Y.; Jin, H.; Jiao, W.; Liu, X.; Yang, W. Metal-organic framework nanosheets as building blocks for molecular sieving membranes. *Science* **2014**, *346*, 1356−1359.
(48) Rodenas, T.; Luz, I.; Prieto, G.; Seoane, B.; Miro, H.; Corma, A.; Kapteijn, F.; Llabrés i Xamena, F. X.; Gascon, J. Metal-organic framework nanosheets in polymer composite materials for gas separation. *Nat. Mater.* **2015**, *14*, 48−55.
(49) Wang, D.; Wang, Z.; Wang, L.; Hu, L.; Jin, J. Ultrathin membranes of single-layered MoS2 nanosheets for high-permeance hydrogen separation. *Nanoscale* **2015**, *7*, 17649−17652.
(50) Berean, K. J.; Ou, J. Z.; Daeneke, T.; Carey, B. J.; Nguyen, E. P.; Wang, Y.; Russo, S. P.; Kaner, R. B.; Kalantar-zadeh, K. 2D MoS2 PDMS Nanocomposites for NO2 Separation. *Small* **2015**, *11*, 5035−5040.
(51) Shen, Y.; Wang, H.; Zhang, X.; Zhang, Y. MoS_2 Nanosheets Functionalized Composite Mixed Matrix Membrane for Enhanced CO_2 Capture via Surface Drop-Coating Method. *ACS Appl. Mater. Interfaces* **2016**, *8*, 23371−23378.
(52) Cornell, W. D.; Cieplak, P.; Bayly, C. I.; Gould, I. R.; Merz, K. M.; Ferguson, D. M.; Spellmeyer, D. C.; Fox, T.; Caldwell, J. W.; Kollman, P. A. A Second Generation Force Field for the Simulation of Proteins, Nucleic Acids, and Organic Molecules. *J. Am. Chem. Soc.* **1995**, *117*, 5179−5197.
(53) Shim, Y.; Jung, Y.; Kim, H. J. Carbon nanotubes in benzene: internal and external solvation. *Phys. Chem. Chem. Phys.* **2011**, *13*, 3969−3978.
(54) Potoff, J. J.; Siepmann, J. I. Vapor-liquid equilibria of mixtures containing alkanes, carbon dioxide, and nitrogen. *AIChE J.* **2001**, *47*, 1676−1682.
(55) Maitland, G. C. *Intermolecular Forces: Their Origin and Determination*; Oxford University Press, 1981.
(56) Plimpton, S. Fast Parallel Algorithms for Short-Range Molecular Dynamics. *J. Comput. Phys.* **1995**, *117*, 1−19.
(57) Straatsma, T. P.; Berendsen, H. J. C. Free energy of ionic hydration: Analysis of a thermodynamic integration technique to evaluate free energy differences by molecular dynamics simulations. *J. Chem. Phys.* **1988**, *89*, 5876−5886.
(58) Shirts, M. R.; Pitera, J. W.; Swope, W. C.; Pande, V. S. Extremely precise free energy calculations of amino acid side chain analogs: Comparison of common molecular mechanics force fields for proteins. *J. Chem. Phys.* **2003**, *119*, 5740−5761.
(59) Abraham, M. J.; Murtola, T.; Schulz, R.; Páll, S.; Smith, J. C.; Hess, B.; Lindahl, E. GROMACS: High performance molecular simulations through multi-level parallelism from laptops to supercomputers. *SoftwareX* **2015**, *1-2*, 19−25.
(60) Azamat, J.; Khataee, A.; Sadikoglu, F. Separation of carbon dioxide and nitrogen gases through modified boron nitride nanosheets as a membrane: insights from molecular dynamics simulations. *RSC Adv.* **2016**, *6*, 94911−94920.
(61) Liu, H.; Cooper, V. R.; Dai, S.; Jiang, D.-e. Windowed Carbon Nanotubes for Efficient CO_2 Removal from Natural Gas. *J. Phys. Chem. Lett.* **2012**, *3*, 3343−3347.
(62) Khakpay, A.; Rahmani, F.; Nouranian, S.; Scovazzo, P. Molecular Insights on the CH_4/CO_2 Separation in Nanoporous Graphene and Graphene Oxide Separation Platforms: Adsorbents versus Membranes. *J. Phys. Chem. C* **2017**, *121*, 12308−12320.
(63) Tian, Z.; Dai, S.; Jiang, D.-e. Expanded Porphyrins as Two-Dimensional Porous Membranes for CO_2 Separation. *ACS Appl. Mater. Interfaces* **2015**, *7*, 13073−13079.

https://dx.doi.org/10.1021/acs.energyfuels.0c00311
Energy Fuels 2020, 34, 7223−7231